Spin-locked transport in a two-dimensional electron gas

S. Anghel,[1,*] F. Passmann,[1,*] K. J. Schiller,[1] J. N. Moore,[2] G. Yusa,[2,3] T. Mano,[4] T. Noda,[4] M. Betz,[1,†] and A. D. Bristow[1,5,‡]

[1]*Experimentelle Physik 2, Technische Universität Dortmund, Otto-Hahn-Straße 4a, D-44227 Dortmund, Germany*
[2]*Department of Physics, Tohoku University, Sendai 980–8578, Japan*
[3]*Center for Spintronics Research Network, Tohoku University, Sendai 980-8578, Japan*
[4]*National Institute for Materials Science, Tsukuba, Ibaraki 305-0047, Japan*
[5]*Department of Physics and Astronomy, West Virginia University, Morgantown, West Virginia 26506-6315, USA*

(Received 12 December 2019; revised manuscript received 31 January 2020; accepted 13 March 2020; published 15 April 2020)

Spin-orbit interactions in solids have inspired innovative physics for spin-based technologies. One such example is the persistent spin helix, where spin-orbit interactions from the semiconductor lattice are balanced with those in asymmetric quantum wells, to create long-lived spin textures. Spin transport in the presence of the momentum-dependent spin-orbit interactions lead to Larmor precession and subsequent dephasing that challenges the design of current spin-based information processing devices. We demonstrate that external magnetic fields can be applied to overcome this issue for spin-polarized charge carriers transported by in-plane electric fields. A frame of reference picture is introduced to describe the emergence and dynamics of the polarization-locked spin-wave packet after optical excitation. Applying well-matched magnetic fields maintains the persistent spin-helix profile regardless of whether the frame of reference is in motion or not. Monte Carlo simulations allow this traveling persistent spin-helix concept to be extended to a proposed spin Hall-effect transistor to ease design requirements.

DOI: 10.1103/PhysRevB.101.155414

I. INTRODUCTION

Persistent spin helices [1] occur in two-dimensional electron gases (2DEG) when the Dresselhaus [2] and Rashba [3] spin-orbit interactions (SOIs) are equal [4]. The combined SOIs manifest themselves as a real-space spin texture that resembles a one-dimensional spin grating [5] arising due to Larmor precession in momentum-dependent effective magnetic fields, $\boldsymbol{B}(\boldsymbol{k})$ [6]. Under these conditions, suppression of D'yakanov-Perel spin dephasing [7] results in significantly long spin coherence times [8], hence the name persistent spin helix (PSH). The adjustable Dresselhaus and Rashba SOIs in low-dimensional systems [9] control the PSH spin texture, such as the periodicity of the spin grating [10], offering functionality to future spintronic devices [11–14]. Moreover, examples like the proposed persistent skyrmion lattice [15] based on coupled orthogonal PSH layers [16] link the nontopological PSH to topological quantum materials [17–20], including topological insulators [21], Weyl semimetals [22,23], and Majorana fermions [24]. Since electron and spin transport are often defining characteristic of devices and topological materials, making control of SOIs in a PSH useful beyond its demonstration.

Practically, the PSH has been observed with transient optical spin-grating measurements [5] or directly using (time-resolved) Kerr-rotation microscopy [25–27]. In the latter, photoexcited spin-polarized carriers created with a tightly focused Gaussian beam undergo diffusive transport, experience precession governed by the SOIs, and relax into the PSH spin-grating mode. This temporal evolution is illustrated in Fig. 1(a) starting from the initial Gaussian at $t = 0$, with the PSH becoming experimentally observable within the spin coherence time $t = \tau_s$, and reaching an ideal spin grating as $t \to \infty$ [28]. In addition to formation of the PSH through diffusion, general control of the spin transport using external electric fields to provide drift velocities for the electrons in the 2DEG [29–31] is desirable for some spintronic applications [13,32,33]. But, this transport introduces k-cubic Dresselhaus effective magnetic fields [27,34–37] that reduce the spin coherence. Generally, dealing with SOI for moving spin-wave packets needs to be addressed if PSHs are wished to be used in spintronic devices, such as a spin Hall-effect (SHE) transistor [13].

In this paper, a traveling PSH (TPSH) is demonstrated with fully controlled SOIs, where drift of a spin-polarized photoexcited carrier distribution is controlled by an in-plane electric field (E_y). This excited spin-wave packet moves relative to the stationary spin texture imposed by the SOIs. The latter can also be set in motion using a concomitant, orthogonal magnetic field (B_x) to match the motion of the spin-polarized carrier distribution (S_z).

II. EXPERIMENT

Sample growth is done by molecular-beam epitaxy on an n-doped GaAs substrate creating a 15-nm GaAs quantum well with $Al_{0.3}Ga_{0.7}As$ barriers. Modulation doping is achieved

*These authors contributed equally to this work.
†markus.betz@tu-dortmund.de
‡alan.bristow@mail.wvu.edu

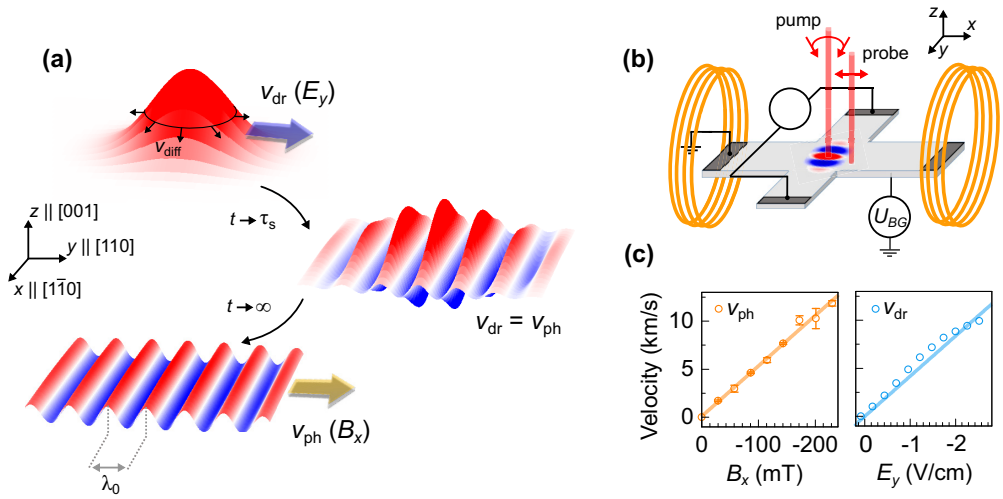

FIG. 1. Controlling transport of the PSH. (a) Schematic evolution of photoexcited Gaussian spin distribution into a homogeneous spin-grating pattern, featuring a single mode with grating period λ_0. Drift (v_{dr}) and phase velocity (v_{ph}) are imposed on the spin carriers and the precession pattern through magnetic and electric fields respectively, following the relations in (c). (b) Experimental sample arrangement, including a schematic pump-probe configuration, Helmholtz coils, and the electrical wiring of the Hall bar contacts which allows for the application of back-gate voltage and in-plane electric field $E_y = U_y/d$. Additional details in Fig. S2 and S4.

by a Si δ layer giving an electron density of $n_0 = 1.3 \times 10^{11}\,\mathrm{cm}^{-2}$, confirmed by photoluminescence and magneto-transport. The sample is processed into a 15-μm-width Hall bar, with a back gate and four-point AuGeNi surface contacts.

Time-resolved (magneto-optic) Kerr rotation microscopy (TR-KRM) is performed with pulses derived from a mode-locked Ti:sapphire laser oscillator, which have independent spatial, temporal, and frequency tuning; see the Supplemental Material [38] (SM) for details of the experiment, theoretical analysis, and additional results. Circular polarized excitation is modulated by an electro-optic modulator (EOM). Reflected linearly polarized probe pulses measure the degree of spin coherence $S_z(x, y, t)$ through balanced-detection polarimetry by a lock-in amplifier referenced to the EOM modulation frequency.

The sample resides in a compact cold-finger cryostat and is cooled to ~4 K. External magnetic fields are applied in the plane of the sample by a pair of Helmholtz coils, where the crystal directions are $x \parallel [1\bar{1}0]$ and $y \parallel [110]$, see Fig. 1(b). In-plane and back-gate fields are applied with voltage sources. The back-gate voltage is set to -1 V, resulting in $\mu_e = 3.8 \times 10^5\,\mathrm{cm}^2/(\mathrm{Vs})$ determined from the TR-KRM.

Numerical simulations are performed with Monte Carlo methods. $S_z(x, y, t)$ is simulated with an ensemble consisting of up to 10^6 spin-carrying electrons, starting with a Gaussian distribution and undergoing Brownian motion [39] in the presence of the SOI-related fields that produce spin precession.

III. RESULTS AND DISCUSSION

By applying an in-plane electric field, the drift velocity is $v_{dr} = -\mu_e E_y$, where μ_e is electron mobility, which resembles a negative pseudo-phase velocity in the spins' moving frame of reference [40]. By contrast, application of B_x is proportional to a real phase velocity (v_{ph}) of the spin texture in the laboratory frame of reference. To create a TPSH, it is proposed that the applied fields set $v_{dr} = v_{ph}$. Corresponding velocity arrows are illustrated in Fig. 1(a). In this case, the TPSH is a PSH in the moving frame of reference. The phase and group velocities associated with the applied in-plane magnetic and electric fields are plotted in Fig. 1(c).

Details of the PSH theoretical framework are given in the SM and lead to a k-dependent effective magnetic field,

$$\boldsymbol{B}_{\mathrm{SOI}}(\boldsymbol{k}) = \frac{2}{g\mu_B}\begin{Bmatrix}[\alpha + (\beta_1 - \beta_3)]k_y \\ [(\beta_1 - \beta_3) - \alpha]k_x\end{Bmatrix}, \tag{1}$$

where $g = 0.3$ is the g factor for the 15-nm-thick modulation-doped GaAs quantum well (QW), μ_B is the Bohr magneton, α is the Rashba SOI parameter, β_1 and β_3 are the linear and cubic Dresselhaus SOI parameters, and k_x and k_y are momenta associated with the x and y crystallographic directions respectively. $\alpha = \gamma_R E_{QW}$, where E_{QW} is the field across the QW and $\gamma_R = 5.26\,\mathrm{meV\,Å}$ is the Rashba coefficient [41]. $\beta_1 = \gamma_D\langle k_z^2\rangle$, where k_z is the out-of-plane wave vector scaled by the QW thickness and $\gamma_D = (9-11)\,\mathrm{meV\,Å}$ [3] is the Dresselhaus coefficient [41]. $\beta_3 = -\gamma_D m^* \epsilon_F/2\hbar^2$, where $m^* = 0.064\,m_e$ is the effective mass and ϵ_F is the Fermi energy.

Equation (1) can be extended to include transport due to both diffusion and drift ($\boldsymbol{k} = \boldsymbol{k}_{\mathbf{diff}} + \boldsymbol{k}_{\mathbf{dr}}$), whose average value is smaller than the Fermi wave number (k_F); see Eq. (S2). This expansion reveals that drift causes a larger spin precession than diffusion when β_3 is not zero [34]. It has been shown that k-cubic SOIs increase with increasing v_{dr} due to electron heating [36,37], because β_3 becomes proportional to the average kinetic energy $\langle\epsilon\rangle$ instead of simply ϵ_F in the degenerate 2DEG case. As a consequence, B_{SOI} deviates from the perfect PSH regime, which when unmodified is defined

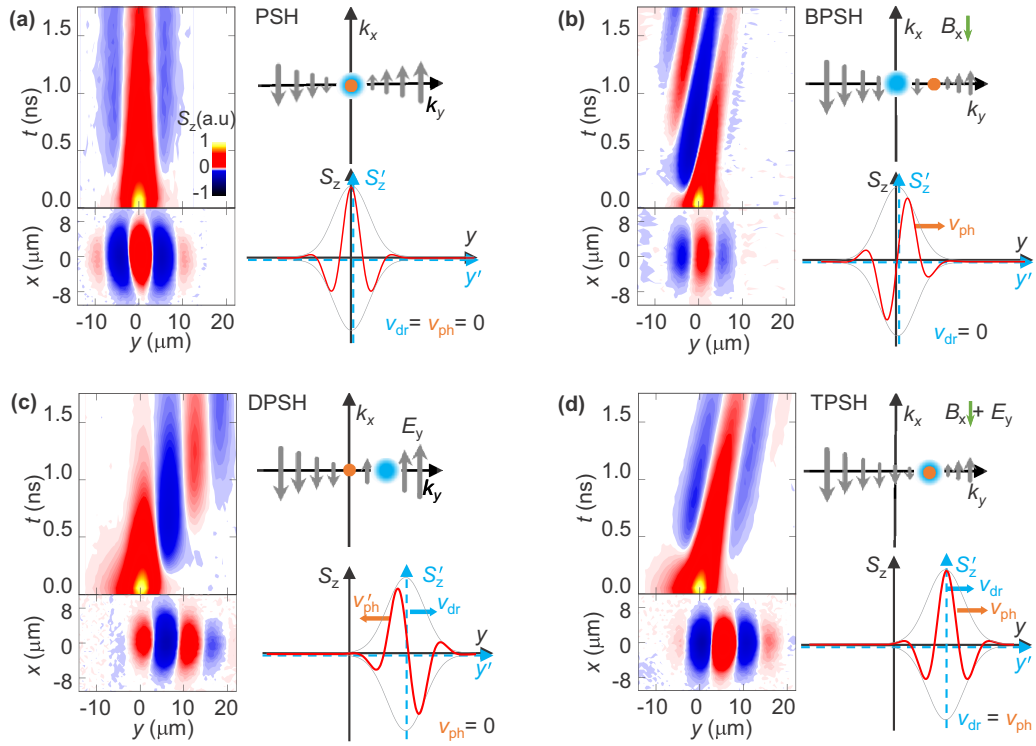

FIG. 2. Dynamics and transport of the spin distribution $S_z(x, y, t)$ with applied external fields. The four panels show experimental space-time results (normalized to the initial intensity) for (a) the stationary persistent spin helix (PSH), (b) the magnetic PSH (BPSH), (c) the drifting PSH (DPSH), and (d) the traveling PSH (TPSH), together with spatial profiles recorded at $t \approx 0.6$ ns for each of the above-mentioned regimes. Additionally, momentum-space schematic diagrams are shown for the four PSH variants, where the arrows indicate the total magnetic field $(B_{\mathrm{SOI},x} + B_x)$, the orange dot is the point without precession, and the blue dot is the excitation position. Furthermore, schemes for the laboratory $S_z(x, y)$ and wave-packet $S_z'(x', y')$ frames of references are shown as well, illustrating the phase v_{ph} and drift v_{dr} velocities color coded for their respective frames of reference.

by the grating periodicity $\lambda_0 = \pi\hbar^2/m^*[\alpha + (\beta_1 - \beta_3)]$ in the y direction. This means that even in samples that have the carrier concentration tuned to reduce β_3 and maximize the spin coherence time, non-negligible k-cubic SOI can occur when an in-plane electric field is applied; details are given for a back-gate voltage of $U_{\mathrm{BG}} = -1$ V in Figs. S3 and S4. In general, a back-gate voltage U_{BG} adjusts α via E_{QW} and β_3 via $\langle\epsilon\rangle$. For devices that wish to exploit drift transport, the drift-induced k-cubic SOI will need to be compensated when moving a spin-wave packet.

In TR-KRM, the spin-sensitive ∼1-μm probe pulse (full width at half maximum) is scanned in the xy plane with respect to the ∼3-μm spin-polarizing pump pulse and as a function of delay time t, such that the resulting measurement can be described as

$$S_z(x, y, t) = A\left\{e^{-[x/w]^2} e^{-[(y-y_{\mathrm{G}})/w]^2}\right\} \cos[2\pi(y - y_{\mathrm{c}})/\lambda], \tag{2}$$

where $y_{\mathrm{G}}(t) = v_{\mathrm{dr}}t$ is the center position of the Gaussian profile resulting from the initiating laser beam of width w_0, $w^2(t)$ is the squared width of the linearly expanding envelope, $\lambda(t) = \lambda_0 w^2(t)/[w^2(t) - w_0^2]$ is the periodicity of the spin grating characterizing the length for a moving spin to undergo one full precession [27], and $y_{\mathrm{c}}(t) = v_{\mathrm{ph}}t$ is the time-varying spatial offset of the spin grating. Without applied in-plane fields, y_{G} and y_{c} do not change, because both v_{dr} and v_{ph} are zero.

Figure 2 explores the dynamics and transport of a PSH in the presence of external fields. Where appropriate, the external fields are $E_y = -0.9$ V/cm and $B_x = -86$ mT. A PSH without the application of any fields in Fig. 2(a) is compared to a PSH in a magnetic field (BPSH) in Fig. 2(b), a PSH drifting due to an electric field (DPSH) in Fig. 2(c), and a DPSH compensated with an external magnetic field leads to the emergence of the desired TPSH in Fig. 2(d). Full $S_z(x, y)$ data for a range of t are presented in Fig. S5 and in Fig. 2 the sets for $t \approx 1.3$ ns are selected, where the effects of drift and phase velocities are seen to work on the spin distribution in the y direction. Direct comparison of the four $S_z(0, y, t)$ data sets, also presented in Fig. 2, makes it clear that with time the PSH wave packet is symmetric and stationary along $y = 0$, while the BPSH develops a stripe pattern that is *slanted* towards $y > 0$ and the DPSH pattern moves towards $y > 0$. Finally for the TPSH, it appears that the PSH shape is recaptured but remains moving towards $y > 0$. Understanding this phenomenon is central to this paper and can be approached in two ways, either by examining a k-space picture of the spin system or a spatial frame of reference picture.

Starting with the k-space picture, in each case of Fig. 2 the momentum-plane diagrams display the average momenta within the spin-wave packet. Spins with increasing k_y experience an increasing $\boldsymbol{B}_{\mathrm{SOI}}$, shown as arrows with increasing magnitude, such that $k_y = 0$ is the only position along the y direction where spins experience no Larmor precession

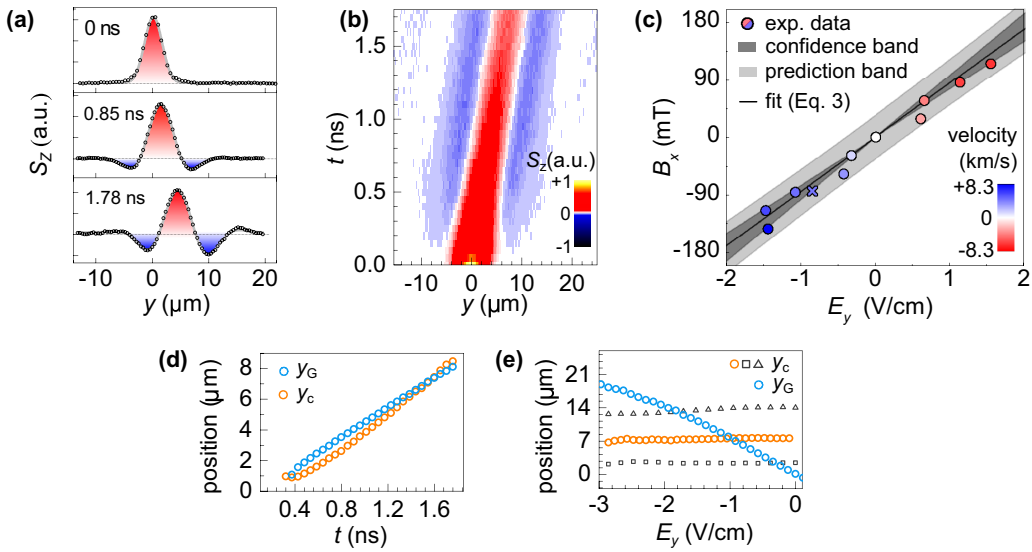

FIG. 3. Conditions and modeling for the TPSH. (a) $S_z(0, y)$ slices of the TPSH for a series of delay times, t, fit with Eq. (1). (b) Monte Carlo simulation of the TPSH normalized to the initial intensity. (c) Experimental points of $v_{ph} \approx v_{dr}$ are overlaid on the theoretical range for the $E_y - B_x$ plane. The cross point indicates the $S_z(0, y, t)$ data shown in Fig. 2. (d) Extracted center of Gaussian, $y_c(t)$, and cosine offset, $y_0(t)$, used to determine phase v_{ph} and drift v_{dr} velocities. (e) Electric field, E_y, dependence of y_c for magnetic-field values of 29, 86, and 144 mT, B_x, compared with the y_0 showing the intersecting points of applied field to produce the TPSH.

(orange dot). In the experiments, the photoexcited spins (blue dot) are also centered at $k_y = 0$ with a finite spread in k due to diffusion. In the case of the BPSH, the superposition of B_x and $B_{SOI,x}$ effectively shifts the zero point of the magnetic field (arrows) and the point of no precession (orange dot) along the y direction (exaggerated in the figure). However, excitation of the spin-wave packet remains at $k_y = 0$ (blue dot), meaning that stationary spins will undergo precession and that spins diffusing along y at an average velocity $\langle v_{diff} \rangle = v_{ph}$ will not. In contrast to the BPSH, the DPSH is essentially the reverse scheme: The point of no precession remains at $k_y = 0$ (orange dot) while the excitation point (blue dot) is not because photoexcited carriers experience drift upon and after excitation. Viewing the BPSH and DPSH in this way, application of appropriate B_x and E_y simultaneously shifts the zero point of the $\boldsymbol{B}_{SOI}$ (arrows), the point of no precession (orange dot), and the excitation point (blue dot), so that they remain overlapped at $k_y \neq 0$. This situation recovers the PSH condition at $k_{dr,y}$ and by compensating for the drift contribution to the effective magnetic field. From Eqs. (S3)–(S5), it can be shown that this compensation occurs when

$$B_x = -\langle B_{SOI,x}(k_y) \rangle = 2(\alpha + \beta_1 - 2\beta_3) m^* \mu_e E_y / g \mu_B \hbar, \quad (3)$$

where the latter expression relates the applied electric and magnetic fields in the case of time-integrated measurements.

Alternatively, the spin-wave packet can be considered from a frame of reference perspective for all cases in Fig. 2. The spin-wave packets are illustrated at a nonzero delay time so that they have evolved to take on characteristics of the spin texture in the y direction of the laboratory frame of reference, $S_z(y)$ (black axes). Given that the PSH evolves symmetrically about the excitation point only due to diffusion, then the wave-packet frame of reference $S'_z(y')$ (blue axes) is identical to the laboratory frame. This is also true for the BPSH, where the laboratory and wave-packet frames both remain stationary, whereas due to v_{ph} the waveform has advanced within the Gaussian envelope. In the DPSH, the laboratory $S_z(y)$ and wave-packet $S'_z(y')$ frames are no longer identical because the wave-packet frame is a moving frame. In this case, the wave packet seems to exhibit a retarded waveform within the Gaussian envelope. In fact, in the moving spin-wave-packet frame the drift velocity of the laboratory frame appears to act as a negative pseudo-phase velocity ($v'_{ph} = -v_{dr}$) on $S'_z(y')$. Hence, phase velocity contributions in the wave-packet frame for the BPSH and DPSH are opposite, confirming Eq. (3). For the TPSH, v_{ph} is matched to the velocity of the moving frame, namely v_{dr}. Consequently, performing the transforms $x' = x$, $y' = y - v_{dr}t$ and $t' = t$ will show that the TPSH profile $S'_z(x', y', t')$ is equivalent to the PSH profile $S_z(x, y, t)$. Hence, the condition $v_{ph} = v_{dr}$ labeling the schematic diagram in Fig. 1(a) refers to the reference frame of the spin-wave packet $S'_z(x', y', t')$, which is a PSH when the velocities are zero and a TPSH when not.

Equation (2) is used to analyze the y-direction slices displayed in Fig. 3(a), from which it is seen that the extracted y_G and y_c coincide throughout the time series [see Fig. 3(d)] to reveal $v_{ph} = (1.00 \pm 0.05) v_{dr}$. Additional $S_z(y, t)$ data for different drift velocities are shown in Fig S6, which are also analyzed to confirm $v_{ph} \approx v_{dr}$. Figure 3(e) shows the extracted $y_c(E_y)$ for a few values of B_x. For the regular PSH, $B_x = 0$ and $v_{ph} = v_{dr} = 0$. Increasing B_x shifts y_c and the associated v_{ph} away from zero, although these lines are independent of E_y. The intercept of y_G and y_c in each case occurs at the point when Eq. (3) is fulfilled and the applied fields appropriately set both the spin-polarized charge carriers and spin texture in motion with the same velocity. These intercept points show the linear relationship between E_y and B_x and are summarized in Fig. 3(c). The experimental data points are fit to Eq. (3) and shown with 95% confidence- and prediction bands to reveal an overall slope that yields $\alpha + \beta_1 - 2\beta_3 = 3.39 \pm 0.3$ meV Å,

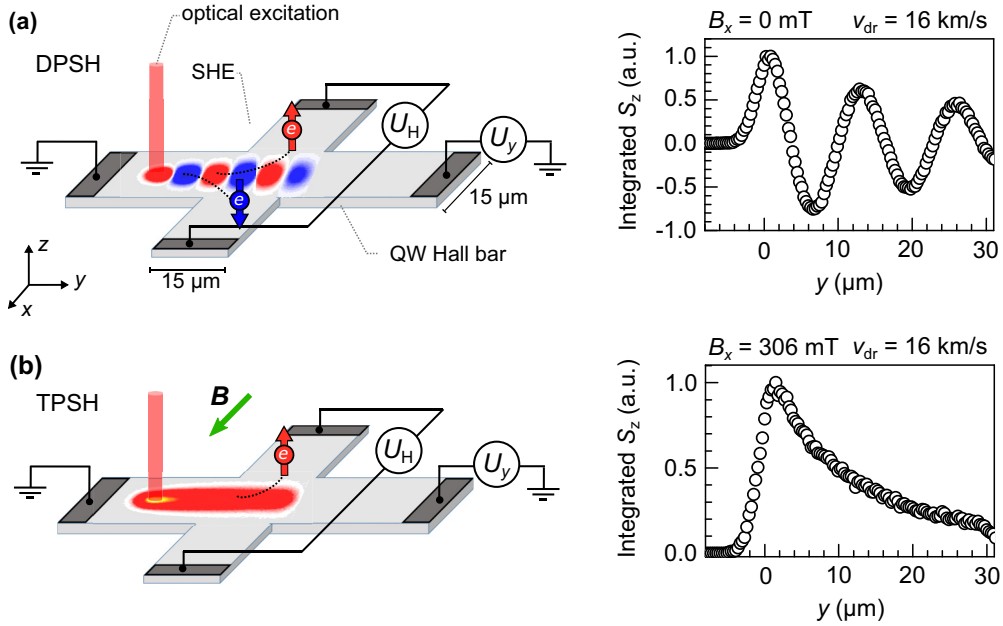

FIG. 4. DPSH and TPSH in a SHE transistor. Continuous optical excitation of (a) DPSH and (b) TPSH into the Hall bar in the presence of an electric field (U_y) that moves the spin-wave packet to the Hall readout (U_H) contact region, where the insets show the spin distribution $S_z(x = 0, y)$, simulated using the Monte Carlo method. The latter exploits the concomitant magnetic field to move the spin texture with a commensurate velocity to that of the spin-wave packet.

which is equivalent to the minimum values independently extracted and shown in Fig. S4(c).

Monte Carlo simulations are used to validate the TPSH results. The experimental $S_z(0, y, t)$ shown in Fig. 2(d) is qualitatively reproduced in Fig 3(b) using the parameters tabulated in Table S1. A complementary series of Monte Carlo simulations matching the experimental data presented in Fig. S6 for a range of drift velocities is also shown in the same figure. By eye, the comparison of the experiments and simulations show excellent qualitative agreement. Moreover, excellent quantitative trends with respect to drift velocity are seen by comparison of the parameters presented in Table S1. Consequently, Monte Carlo simulations can reliably be used to explore devices based on the TPSH.

How can the TPSH influence spintronic devices? Electron spins have several useful attributes for information processing, including energy-efficient switching, the inherent *quantumness* of the two-level spin-1/2 system from which "qubits" can be constructed, and direct coupling to circular-polarized light for interfacing with photonics. Work focused on *in situ* reading and writing to spin systems has inspired devices like the Datta-Das spin transistor [32]. Nonetheless, spintronic devices that make use of spin transport will require long coherence times and control of the SOIs; hence, understanding the PSH in a moving frame of reference is insightful. To see this in practice, let us consider a spin Hall-effect transistor based on the one proposed by Wunderlich *et al.* [13]. Figure 4(a) shows a design of a SHE transistor that exploits a continuously photoexcited spin-wave packet emanating from the excitation location and drifting to the readout location where a transverse Hall voltage (U_H) is measured, because spin-*up* electrons move towards one transverse contact and spin-*down* electrons move towards the other. The Monte Carlo simulation is produced by time-integrating individual time slices, resulting in a spin-wave packet that resembles a DPSH with periodicity in the y direction of the stationary PSH mode. Each point along the drift direction comprises spins that on average have undergone the same Larmor precession. In this example, a fixed distance between the excitation and readout locations will always result in the same sign of the spin polarization and if that distance happens to fall at the node of the spin texture, no signal will be seen at all. Moreover, the width of the readout channel is required to be smaller than the spin texture, namely $<\lambda_0/2$, to prevent canceling of positive and negative contributions from the DPSH. Furthermore, the k-cubic Dresselhaus SOI contributions have been identified to hinder cohesive transport of a spin-wave packet due to polarization smearing leading to a reduction in the signal-to-noise ratio [34].

In contrast, using a TPSH in the same continuously excited SHE transistor results in the spin-wave packet and the texture moving together, so that spins are locked to a single direction when deviated by the SHE; see the schematic diagram in Fig. 4(b). Here, the initial spin-polarization direction visibly dominates over the full range of drift. However, compared to a case without any SOI, the summed polarization is diminished due to spin precession caused by diffusion. The TPSH-based SHE transistor can then operate with arbitrary location and width of the readout location, because the net spin polarization remains unidirectional as the wave packet emanates from the excitation location, as illustrated by the Monte Carlo simulation. The result would ease constraints on excitation and readout locations and readout electronics speeds. In the scheme exploiting the TPSH, the transistor states can be simply slaved to the excitation polarization, linking photonics and spintronics and providing a platform

for multiple Hall readouts. Using a TPSH in the y direction can be added to dynamic transport schemes in the entire xy plane [35] and overcome any lateral diffusive spin precession that occurs when transporting along the x direction [37,42]. Finally, the discussion of Eq. (3) shows that drift-induced SOI contributions are compensated along the drift direction by the application of an external magnetic field, although it is unclear whether spin decoherence or k-cubic SOI contributions [34] can be altered and requires further study in systems that have demonstrated ways to asses spin decay mechanism with applied external fields [43].

IV. CONCLUSION

The proposed TPSH-based SHE transistor and the demonstration of TPSH in a GaAs 2DEG show promise for SOI control in future spintronic devices and provide a window into control of materials and heterostructures that exhibit conventional and topological dependence on their spin transport. The simultaneous use of orthogonal in-plane electric and magnetic fields specifically moves photoexcited spin-polarized charge carriers in concert with the underlying spin texture of the system. One benefit is the compensation for drift-induced SOIs along the spin transport direction that are otherwise problematic for spintronic device design.

ACKNOWLEDGMENTS

The authors wish to thank Alexander Poshakinskiy and Sergey Tarasenko from the Ioffe Institute for extensive useful discussions and Cheng Cen and Tudor Stanescu at West Virginia University for additional discussions. Funding was provided by the Deutsche Forschungsgemeinschaft International Collaborative Research Centre TRR-160 (B3) (Project No. 249492093), a Grant-in-Aid for Scientific Research (Grant No. 17H01037) from the Ministry of Education, Culture, Sports, Science, and Technology (MEXT), Japan, and the Asahi Glass Foundation.

[1] B. A. Bernevig, J. Orenstein, and S. C. Zhang, Phys. Rev. Lett. **97**, 236601 (2006).
[2] G. Dresselhaus, Phys. Rev. **100**, 580 (1955).
[3] E. I. Rashba, Fiz. Tverd. Tela **2**, 1224 (1960) [Sov. Phys. Solid State **2**, 1109 (1960)].
[4] T. D. Stanescu and V. Galitski, Phys. Rev. B **75**, 125307 (2007).
[5] J. D. Koralek, C. P. Weber, J. Orenstein, B. A. Bernevig, S.-C. Zhang, S. Mack, and D. D. Awschalom, Nature (London) **458**, 610 (2009).
[6] J. Schliemann, Rev. Mod. Phys. **89**, 011001 (2017).
[7] M. I. Dyakono and V. I. Perel, Zh. Eksp. Teor. Fiz. **13**, 657 (1971) [Sov. Phys. JETP Lett. **13**, 467 (1971)].
[8] P. Altmann, M. P. Walser, C. Reichl, W. Wegscheider, and G. Salis, Phys. Rev. B **90**, 201306(R) (2014).
[9] A. Soumyanarayanan, N. Reyren, A. Fert, and C. Panagopoulos, Nature (London) **539**, 509 (2016).
[10] F. Dettwiler, J. Y. Fu, S. Mack, P. J. Weigele, J. C. Egues, D. D. Awschalom, and D. M. Zumbuhl, Phys. Rev. X **7**, 031010 (2017).
[11] I. Žutić, J. Fabian, and S. Das Sarma, Rev. Mod. Phys. **76**, 323 (2004).
[12] D. D. Awschalom and M. E. Flatté, Nat. Phys. **3**, 153 (2007).
[13] J. Wunderlich, B.-G. Park, A.C. Irvine, L.P. Zârbo, E. Rozkotová, P. Nemec, V. Novák, J. Sinova, and T. Jungwirth, Science **330**, 1801 (2010).
[14] D. D. Awschalom, L. C. Bassett, A. S. Dzurak, E. L. Hu, and J. R. Petta, Science **339**, 1174 (2013).
[15] J. Fu, P. H. Penteado, M. O. Hachiya, D. Loss, and J. C. Egues, Phys. Rev. Lett. **117**, 226401 (2016).
[16] M. Luengo-Kovac, F. C. D. Moraes, G. J. Ferreira, A. S. L. Ribeiro, G. M. Gusev, A. K. Bakarov, V. Sih, and F. G. G. Hernandez, Phys. Rev. B **95**, 245315 (2017).
[17] A. Manchon, H. C. Koo, J. Nitta, S. M. Frolov, and R. A. Duine, Nat. Mater. **14**, 871 (2015).
[18] Moh. Adhib Ulil Absor and F. Ishii, Phys. Rev. B **99**, 075136 (2019).
[19] P. Li, W. Wu, Y. Wen, C. Zhang, J. Zhang, S. Zhang, Z. Yu, S. A. Yang, A. Manchon, and X. Zhang, Nat. Commun. **9**, 3990 (2018).
[20] B. Keimer and J. E. Moore, Nat. Phys. **13**, 1045 (2017).
[21] M. Z. Hasan and C. L. Kane, Rev. Mod. Phys. **82**, 3045 (2010).
[22] S. A. Yang, SPIN **06**, 1640003 (2016).
[23] N. P. Armitage, E. J. Mele, and A. Vishwanath, Rev. Mod. Phys. **90**, 015001 (2018).
[24] V. Mourik, K. Zuo, S. M. Frolov, S. R. Plissard, E. P. A. M. Bakkers, and L. P. Kouwenhoven, Science **336**, 1003 (2012).
[25] M. P. Walser, C. Reichl, W. Wegscheider, and G. Salis, Nat. Phys. **8**, 757 (2012).
[26] M. Kohda, V. Lechner, Y. Kunihashi, T. Dollinger, P. Olbrich, C. Schönhuber, I. Caspers, V. V. Bel'kov, L. E. Golub, D. Weiss, K. Richter, J. Nitta, and S. D. Ganichev, Phys. Rev. B **86**, 081306(R) (2012).
[27] S. Anghel, F. Passmann, A. Singh, C. Ruppert, A. V. Poshakinskiy, S. A. Tarasenko, J. N. Moore, G. Yusa, T. Mano, T. Noda, X. Li, A. D. Bristow, and M. Betz, Phys. Rev. B **97**, 125410 (2018).
[28] G. Salis, M. P. Walser, P. Altmann, C. Reichl, and W. Wegscheider, Phys. Rev. B **89**, 045304 (2014).
[29] D. Hägele, M. Oestreich, W. W. Rühle, N. Nestle, and K. Eberl, Appl. Phys. Lett. **73**, 1580 (1998).
[30] M. Furis, D. L. Smith, S. Kos, E. S. Garlid, K. S. M. Reddy, C. J. Palmstrøm, P. A. Crowell, and S. A. Crooker, New J. Phys. **9**, 347 (2007).
[31] L. Nadvornik, P. Nemec, T. Janda, K. Olejnik, V. Novak, V. Skoromets, H. Nemec, P. Kuzel, F. Trojanek, T. Jungwirth, and J. Wunderlich, Sci. Rep. **6**, 22901 (2016).
[32] S. Datta and B. Das, Appl. Phys. Lett. **56**, 665 (1990).
[33] A. V. Kuhlmann, J. Houel, A. Ludwig, L. Greuter, D. Reuter, A. D. Wieck, M. Poggio, and R. J. Warburton, Nat. Phys. **9**, 570 (2013).

[34] P. Altmann, F. G. G. Hernandez, G. J. Ferreira, M. Kohda, C. Reichl, W. Wegscheider, and G. Salis, Phys. Rev. Lett. **116**, 196802 (2016).

[35] Y. Kunihashi, H. Sanada, H. Gotoh, K. Onomitsu, M. Kohda, J. Nitta, and T. Sogawa, Nat. Commun. **7**, 10722 (2016).

[36] Y. Kunihashi, H. Sanada, Y. Tanaka, H. Gotoh, K. Onomitsu, K. Nakagawara, M. Kohda, J. Nitta, and T. Sogawa, Phys. Rev. Lett. **119**, 187703 (2017).

[37] F. Passmann, A. D. Bristow, J. N. Moore, G. Yusa, T. Mano, T. Noda, M. Betz, and S. Anghel, Phys. Rev. B **99**, 125404 (2019).

[38] See Supplemental Material at http://link.aps.org/supplemental/10.1103/PhysRevB.101.155414 for experimental setup, sample characterization, Monte Carlo simulation, and additional spin transport results.

[39] A. V. Poshakinskiy and S. A. Tarasenko, Phys. Rev. B **92**, 045308 (2015).

[40] Y. Tanaka, Y. Kunihashi, H. Sanada, H. Gotoh, K. Onomitsu, M. Kohda, J. Nitta, and T. Sogawa, Appl. Phys. Express **12**, 013001 (2018).

[41] F. Passmann, S. Anghel, C. Ruppert, A. Bristow, A. Poshakinskiy, S. A. Tarasenko, and M. Betz, Semicond. Sci. Technol. (2019).

[42] T. Saito, A. Aoki, J. Nitta, and M. Kohda, Appl. Phys. Lett. **115**, 052402 (2019).

[43] G. J. Ferreira, F. G. G. Hernandez, P. Altmann, and G. Salis, Phys. Rev. B **95**, 125119 (2017).